Title

âBreathingâ organic cation to stabilize multiple structures in low-dimensional Ge-, Sn-, and Pb-based hybrid iodide perovskites

Journal

Inorganic Chemistry Frontiers, 9(19)

ISSN

2052-1553

Authors

Chen, Congcong
Morgan, Emily E
Liu, Yang
et al.

Publication Date

2022

DOI

10.1039/D2QI01247B

Peer reviewed

ARTICLE

"Breathing" organic cation to stabilize multiple structures in low-dimensional Ge-, Sn-, and Pb-based hybrid iodide perovskites

Received 00th January 20xx,
Accepted 00th January 20xx

DOI: 10.1039/x0xx00000x

Congcong Chen,[a] Emily E. Morgan,[b] Yang Liu,[a] Jian Chen,[a] Ram Seshadri[b] and Lingling Mao*[a]

Low-dimensional hybrid inorganic–organic perovskites are candidates for stable optoelectronic devices. The dimensionality of these perovskites depends largely on the organic and inorganic compositions, as well as the synthetic conditions. Here, we report five new hybrid iodides, $(ETU)_4Ge_5I_{18}$, $(ETU)GeI_4$, $(ETU)SnI_4$, $(ETU)PbI_4$, and $(ETU)_3Pb_2I_{10}$ using only one type of organic cation, namely, S-(2-Aminoethyl)isothiouronium (ETU). $(ETU)GeI_4$ and $(ETU)SnI_4$ belong to the (110)-oriented structure-type with "3 × 3" sawtooth corrugated layers and crystallize in a structure with the orthorhombic space group *Pbca*. $(ETU)_4Ge_5I_{18}$ crystallizes in a structure with the triclinic space group *P*-1, featuring a 2D layered structure with combinations of corner, edge, and face-sharing $[GeI_6]$ octahedra. For the Pb-based series, $(ETU)PbI_4$ has the conventional (100)–oriented 2D type whereas $(ETU)_3Pb_2I_{10}$ has a unique 0D structure. Remarkably, the unstable 2D orange-phase $(ETU)PbI_4$, transforms to a stable 0D yellow phase $(ETU)_3Pb_2I_{10}$, accompanied by the reduction of the C-S-C angle of the organic cation ETU. The optical band gaps are largely regulated by the diverse types of structure and are in the range of 1.8 eV to 2.8 eV. $(ETU)SnI_4$ is the only material showing notable photoluminescence at room-temperature. Our work showcases the flexibility of the organic cation in determining the structural dimensionality and provides a new strategy in generating new hybrid materials.

Introduction

Hybrid halide perovskite materials with small exciton binding energy, high carrier lifetime, high absorption coefficient and other favorable properties have been extensively studied for optoelectronic applications.[1-6] Three-dimensional (3D) halide perovskites have a general formula of AMX_3 (A = Cs^+, $CH_3NH_3^+$, $HC(NH_2)_2^+$; M = Pb, Sn or Ge; X = halide),[4,7,8] for a limited set of *A*-site cations. In contrast, low-dimensional perovskites enjoy tremendous chemical flexibility as well as structural diversity, offering the opportunity to use a large variety of functional organic molecules as cations.[9-12] 2D perovskites can be obtained via chemically sectioning the 3D perovskite lattice along different planes, resulting in (100)-, (110)- and (111)-oriented perovskites, which have layered or corrugated sheets that are sandwiched between large organic cations.[9,13,14] Other derivatives with lower dimensionality such as 1D or 0D structures often consist of edge-shared or face-shared octahedra.[15,16] The reduction of dimensionality in these materials has an enormous influence on their physical and optoelectronic properties, leading to other specific applications.[17,18]

A promising strategy for novel functional hybrid materials is to combine the properties of the inorganic frameworks with the functionality and flexibility of the organic component. Especially for 2D perovskites, the selection of cations has a great influence on the formation of different types of layers such as (110)-oriented layered types. These "sawtooth" (110) -oriented 2D perovskites are named "n×n", where n represents the number of octahedra that form half of the sawtooth, thus these structures can be regarded as "2 × 2", "3 × 3", "4 × 4", etc.[19] Previously, the "2 × 2" structural type has been extensively studied.[20-22] In the case of the "3 × 3" type, α-$(DMEN)PbBr_4$ (DMEN = 2-(dimethylamino)ethylamine) was the first example, and was constituted of alternating rows of *cis* and *trans* octahedra.[19] Recently, Tremblay *et al*. have reported a new "3 × 3" corrugated 2D hybrid perovskite, $(4NPEA)_2PbI_4$ (4NPEA = 4-nitrophenylethylammonium), demonstrating that the optical property is similar to other 2D perovskites with distorted $[PbI_6]$ octahedra.[23] Guo *et al*. have further reported that [ImH][TzH]$PbBr_4$, ($[ImH^+]$ = imidazolium, $[TzH^+]$ = 1,2,4-triazolium), adopting a "3 × 3" structural type, is the first example of a bromide perovskite incorporating two types of ordered organic cations.[24] Other similar "3 × 3" corrugated 2D Pb-based perovskites have also been reported and employed in solar cell devices.[25] In contrast, the Sn-based "3 × 3" corrugated 2D perovskites are much rarer, with the only example being $(ImEA)[SnI_4]$ ($ImEA^{2+}$ = 1-(2-ammonioethyl)-1H-imidazol-3-ium).[26] For the "4 × 4" corrugated structures, α-$[NH_3(CH_2)_5NH_3]SnI_4$[27] and α-$(HA)SnI_4$[28] are the only two

[a] *Department of Chemistry, Southern University of Science and Technology Shenzhen, Guangdong 518055, China Email: maoll@sustech.edu.cn*
[b] *Materials Research Laboratory and Materials Department, University of California, Santa Barbara, California 93106, United States Email: seshadri@mrl.ucsb.edu*
†Electronic Supplementary Information (ESI) available. See DOI: 10.1039/x0xx00000x

examples reported. An additional consideration in our work is that most reports on hybrid halide perovskites have mainly focused on Pb- and Sn-based phases. Within the same group, Ge^{2+} has a similar electron configuration of Sn^{2+} and Pb^{2+}, and significant effect of its lone pair.[29] However, Ge-based phases are much less explored.[30,31]

Here, by using S-(2-aminoethyl)isothiouronium (ETU) as the organic templating cation, five new hybrid iodides, namely $(ETU)_4Ge_5I_{18}$, $(ETU)GeI_4$, $(ETU)SnI_4$, $(ETU)PbI_4$ and $(ETU)_3Pb_2I_{10}$, are reported. $(ETU)GeI_4$ and $(ETU)SnI_4$ are structurally analogous, featuring interesting corrugated "3 × 3" layered structures which belong to the (110)-oriented 2D perovskite family. $(ETU)GeI_4$ represents the first Ge-based example of the "3 × 3" type of corrugated sawtooth 2D perovskite. A different structure, $(ETU)_4Ge_5I_{18}$, is also obtained by controlling the reaction ratio of the precursor organic cation and the inorganic precursors. Interestingly, an orange phase 2D perovskite $(ETU)PbI_4$ can be further converted to the yellow phase 0D structure $(ETU)_3Pb_2I_{10}$, with the reduction of the C-S-C angle of the sulfur-containing ammonium cation ETU. The above compounds have optical band gaps in the range of 1.8-2.8 eV, which can be tuned with varying structural types and octahedral connectivity. At room-temperature, only $(ETU)SnI_4$ exhibits photoluminescence (PL), which could be due to the relatively stable configuration since it is the only material with just one structure (Ge and Pb each have two). This work demonstrates the utility of flexible organic cations in dictating a range of hybrid structures that are significant in the development of materials for advanced optoelectronic applications.

Experimental

Synthesis

All chemicals were purchased from Sigma-Aldrich and used without further purification or modification.

$(ETU)_4Ge_5I_{18}$ and $(ETU)GeI_4$. GeO_2 (0.1 g, 1 mmol) powder was dissolved in 47% hydriodic acid (8.0 mL) and 50% aqueous H_3PO_2 (1.5 mL) by heating under stirring for 30 min at 127 °C until the solution clarified. Then, S-(2-aminoethyl)isothiouronium bromide hydrobromide (0.168 g, 0.8 mmol) was added to the above solution under heating and stirring for an additional 5 min. Yellow needle crystals of $(ETU)_4Ge_5I_{18}$ precipitated during slow cooling. Orange plate crystals of $(ETU)GeI_4$ were formed in the same fashion except the ratio of S-(2-aminoethyl)isothiouronium bromide hydrobromide (0.281 g, 1 mmol) to GeO_2 (0.1 g, 1 mmol) was enlarged to 1:1.

$(ETU)SnI_4$. $SnCl_2{\cdot}2H_2O$ (0.225 g, 1 mmol) powder was dissolved in 47% hydriodic acid (8.0 mL) and 50% aqueous H_3PO_2 (1.5 mL) by heating under stirring for 10 min at 127 °C until the solution turned light yellow. Then S-(2-aminoethyl)isothiouronium bromide hydrobromide (0.281 g, 1 mmol) was added to the above solution, and the resultant mixture was stirred and heated for 5 min. Dark red plate-like crystals precipitated during slow cooling.

$(ETU)PbI_4$ and $(ETU)_3Pb_2I_{10}$. PbO (0.223 g, 1 mmol) powder was dissolved in 47% hydriodic acid (4.0 mL) and 50% aqueous H_3PO_2 (1.0 mL) by heating under stirring for 5 min at 127 °C until the solution turned bright yellow. Then S-(2-aminoethyl)isothiouronium bromide hydrobromide (0.281 g, 1 mmol) was added to the above solution, and the resultant mixture was evaporated to approximately at half its original volume by stirring and heating. The solution was then left to stand overnight and allowed to crystallize into orange block crystals $(ETU)PbI_4$ at room temperature. However, the orange phase $(ETU)PbI_4$ is unstable. After removing a part of the crystals in the mother liquid, all of the orange block crystals in contact with the mother liquid quickly changed to yellow block crystals. Similarly, orange block crystals placed in the air also turned to yellow block crystals about one hour. Similar synthetic approaches were used to directly synthesize the yellow block crystals $(ETU)_3Pb_2I_{10}$ except S-(2-aminoethyl)isothiouronium bromide hydrobromide (0.562 g, 2 mmol) to PbO (0.223 g, 1 mmol) ratio was doubled to 2:1.

Single Crystal X-ray Diffraction

The single-crystal diffraction data was collected on a Bruker APEX-II CCD diffractometer for $(ETU)SnI_4$ and $(ETU)_3Pb_2I_{10}$ at 298 K, as well as on a Bruker D8 Venture diffractometer for $(ETU)GeI_4$, $(ETU)_4Ge_5I_{18}$ at 298 K and $(ETU)PbI_4$ at 100 K using Mo-Kα (λ=0.71073 Å) radiation. The data collection and reduction were carried out using the Bruker APEX3 program for all compounds.[32] The crystal structures were solved by direct method and refined using the OLEX2 program package based on F^2 with refinements of full-matrix least-squares.[33,34] All the non-hydrogen atoms were refined with anisotropic thermal parameters. The hydrogen atoms attached to C and N atoms of organic molecules were positioned geometrically and refined isotropically. The data has been deposited in the CCDC database under 2169490-2169494.

Powder X-ray Diffraction (PXRD)

The powder X-ray diffraction (PXRD) data were collected on SmartLab X-ray Diffractometer (Cu-Kα, λ = 1.54056 Å) at a voltage of 45 kV and a current of 200 mA in the range of 5−50° with the step size of $10°{\cdot}min^{-1}$ to confirm the purity of each sample at room temperature. By using the crystallographic file from the single-crystal X-ray diffraction experiment, the simulated powder pattern was calculated via Mercury software.

Optical Absorption Spectroscopy

The solid UV-Vis absorbance spectra were recorded at room temperature on a Shimazu UV-3600i Plus spectrophotometer with $BaSO_4$ as the reference substance with the wavelength range at 200 nm to 900 nm. The reflectance spectra were converted to absorption spectra according to the Kubelka-Munk function: $\alpha/S = F(R) = (1-R)^2/2R$, where S is the scattering coefficient, α is the absorption coefficient, and R is the reflectance.[35]

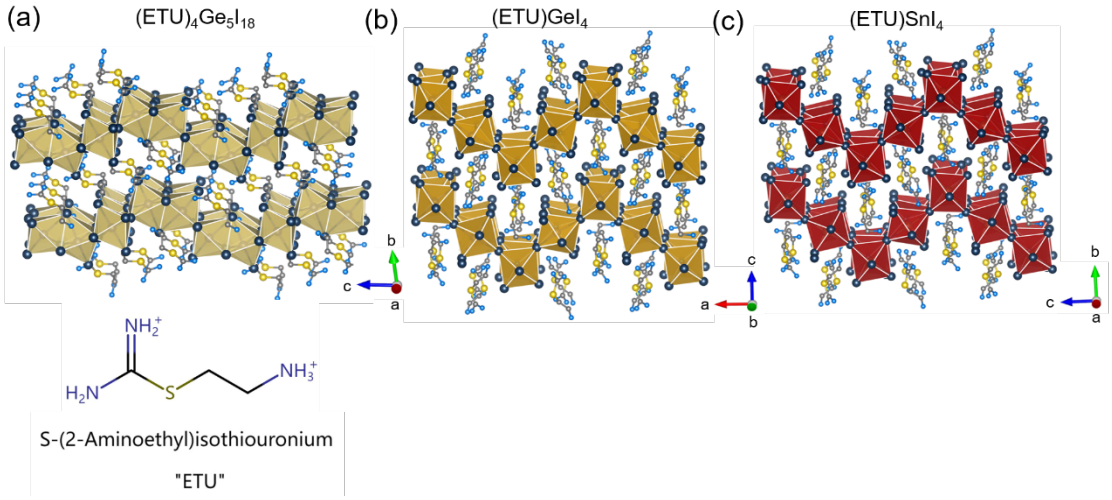

Fig. 1 Crystal structures of (a) $(ETU)_4Ge_5I_{18}$, (b) $(ETU)GeI_4$, and (c) $(ETU)SnI_4$ and structure of the organic cation used here. Elements indicated by: dark blue (I), yellow (S), blue (N), dark gray (C). All hydrogen atoms are omitted for clarity.

Steady-State Photoluminescence (PL)

Steady-state PL spectra were conducted on LabRAM HR Evolution Laser Confocal Micro-Raman Spectroscopy at room temperature with 532 nm laser.

Computational Details.

Density functional theory (DFT) calculations were performed using the Vienna Ab initio Simulation Package[36-38] (VASP), version 5.4.4. The Perdew-Burke-Ernzerhof[39] (PBE) functional and projector-augmented wave[40,41] (PAW) pseudopotentials were used with a plane-wave cut-off energy of 700 eV and energy convergence of 10^{-5} eV or better. PAW potentials were chosen following the version 5.2 guidelines. Automatic k-mesh generation[42] was used with a length parameter (R_k) of 40 or better. Spin-orbit coupling corrections were included for the Pb-based structures. For band-structure calculations, an appropriate **k**-path was generated using SeeK-path.[43,44] Density of states were plotted and analysed using Sumo.[45,46]

Results and discussion

Unlike the relatively common perovskite-like organic-inorganic hybrids formed by rigid cations, a flexible organic cation can lead to richer and more diverse structures. The flexible cation ETU used here forms two different compounds with Ge and Pb, respectively, and one layered compound with Sn. The crystal structures of all five compounds are shown in Fig. 1 and 2, and crystallographic data are tabulated in Table S1 and S2. $(ETU)_4Ge_5I_{18}$ crystallizes in the triclinic space group *P*-1, and the inorganic sheets consist of mixed corner-sharing, edge-sharing and face-sharing $[GeI_6]$ octahedra (Fig. 1a and S2). $(ETU)GeI_4$ crystallizes in a structure with the orthorhombic space group *Pbca*. It adopts a layered structure templated by the divalent organic cation, where each layer is formed with corner-sharing of $[GeI_6]$ octahedra resulting in a "3 × 3" type of sawtooth corrugated structure (Fig. 1b). This is the first example of "3 × 3" corrugated 2D Ge-based perovskite. $(ETU)SnI_4$ is structurally analogous to $(ETU)GeI_4$ (Fig. 1c). We

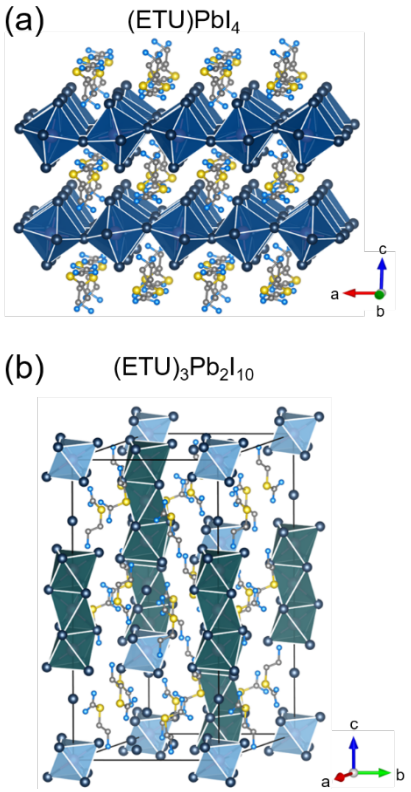

Fig. 2 Crystal structures of (a) $(ETU)PbI_4$ and (b) $(ETU)_3Pb_2I_{10}$. Elements indicated by: dark blue (I), yellow (S), blue (N), dark grey (C). Shown also are the metal halide units including distorted octahedra (light blue) and trimer octahedra (dark green) for $(ETU)_3Pb_2I_{10}$. All H atoms are omitted for clarity.

further quantified the individual distortion of the octahedra for $[GeI_6]$ and $[SnI_6]$ by determining the bond length distortion (Δd) and octahedral angle variance (σ^2) listed in Table S3 (calculated using VESTA software). We note that the average Δd (3.18×10^{-2}) and average σ^2 (12.76) for $(ETU)SnI_4$ is less than the value of $(ETU)GeI_4$, where the larger radius of Sn compared to that of Ge

accounts for the smaller distortion in the Sn analogue. The octahedral distortion index Δd for all three individual [PbI_6] in $(ETU)_3Pb_2I_{10}$ is either zero or close to zero, which indicates the stable nature of the compound and the higher tolerance for the 0D structure.

For the Pb-based materials, $(ETU)PbI_4$ crystallizes in a structure with the monoclinic space group $P2_1/c$, featuring the conventional (100)-oriented 2D structure with corner-sharing [PbI_6] octahedra (Fig. 2a). The Br analogue $(ETU)PbBr_4$ has been previously reported by Kundu *et al* and belongs to the (110)-oriented type.[47] $(ETU)_3Pb_2I_{10}$ crystallizes in the trigonal space group *R*-3, where the isolated [PbI_6] octahedra and $[Pb_3I_{12}]^{6-}$ trimer are surrounded by ETU cations and iodide anions, giving rise to an 0D structure (Fig. 2b and S3). Interestingly, the 2D orange phase $(ETU)PbI_4$ can be transformed to the stable 0D yellow phase $(ETU)_3Pb_2I_{10}$ when the concentration of the mother liquor is low or exposed in air. This conversion is irreversible.

More interestingly, the degree of cations torsion angle (C-S-C angle) also varies in different structures. One can easily see from Fig. 3a and 3b that degree of cation distortion is changed in the two distinct 2D Ge-based structures. The torsion angles of the C-S-C in $(ETU)_4Ge_5I_{18}$ structure are 100° and 102.5° (Fig 3b), respectively, whereas the torsion angles of the C-S-C are106.4° and 103.4° in the $(ETU)GeI_4$ structure (Fig 3a). In Pb-based series, there are two different conformational cations with the C-S-C torsion angles of 105.5° and 103.1° within the 2D orange phase $(ETU)PbI_4$ (Fig. 3c). Owing to the inherent flexibility of the cations in the crystal structure, the cation has only one configuration in the 0D phase, with the C-S-C torsion angle of 103.9° (Fig. 3d). Generally speaking, the yellow phases $(ETU)_4Ge_5I_{18}$ and $(ETU)_3Pb_2I_{10}$ with smaller C-S-C angles are more stable than the orange phases $(ETU)GeI_4$ and $(ETU)PbI_4$. The dynamic movement of ETU cations reaches a final state, where the yellow phases are stabilized.

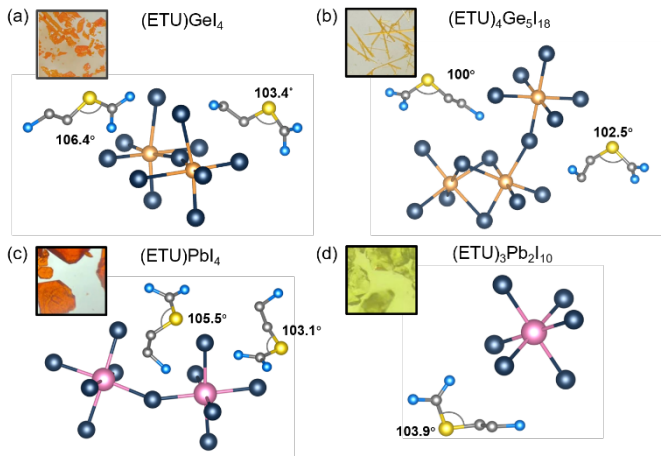

Fig. 3 The layout of cationic entities in the structures of (a) $(ETU)GeI_4$, (b) $(ETU)_4Ge_5I_{18}$, (c) $(ETU)PbI_4$, (d) and $(ETU)_3Pb_2I_{10}$. Elements indicated by: orange (Ge), pink (Pb), dark blue (I), yellow (S), blue (N), dark gray (C), and all H atoms are omitted here for clarity. Inserted: optical microscope picture of corresponding single crystals.

Differences in the structure remarkably affect the photophysical properties of these materials. The optical band gaps of the five compounds reported here were determined by diffuse reflectance UV−vis spectroscopy measurements (Fig. 4a). These materials all show clear excitonic features close to the band edges. $(ETU)_4Ge_5I_{18}$ has a band gap of 2.30 eV, with an average Ge−I−Ge angle of 111.2°, while $(ETU)GeI_4$ has a slightly smaller band gap (2.14 eV), due to a larger averaged angle of 162.3°. These hybrid germanium iodides, reasonably have narrower band gaps compared with reported 2D Ge-Br perovskites.[31] $(ETU)SnI_4$ has the narrowest band gap of the series (1.87 eV), which is consistent with band gap value of α-$(HA)SnI_4$ with "4 × 4" corrugated structure.[28] Within the Pb series, $(ETU)PbI_4$ with the 2D structure has the lower band gap of 2.17 eV while $(ETU)_3Pb_2I_{10}$ with the 0D structure has higher band gap (2.71 eV) because the later has lower dimensionality. These two phases are easily distinguishable by color, which are consistent with previously reported.[16,48]

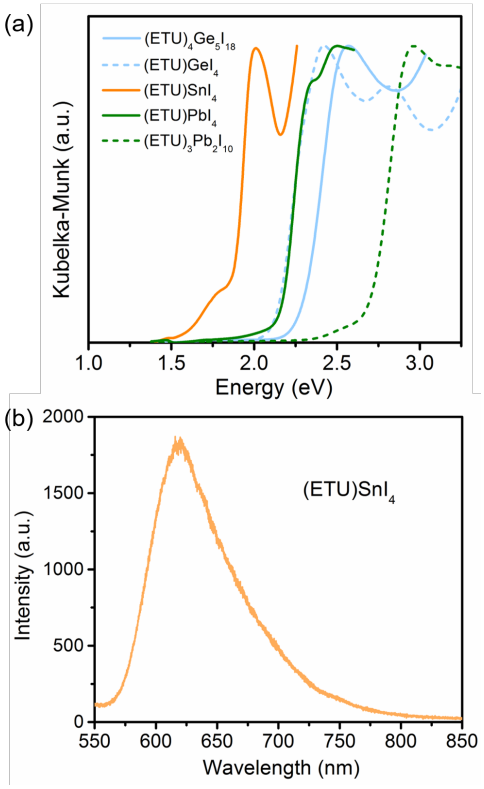

Fig. 4 (a) UV−vis absorption spectra of $(ETU)_4Ge_5I_{18}$, $(ETU)GeI_4$, $(ETU)SnI_4$, $(ETU)PbI_4$ and $(ETU)_3Pb_2I_{10}$ at room temperature. (b) Steady-state photoluminescence (PL) spectra (excited at 532 nm) for $(ETU)SnI_4$ at room temperature.

To further evaluate the optical properties of these materials, we performed photoluminescence (PL) measurements on single crystals at room temperature. Unfortunately, no significant emission peaks were observed in Ge-and Pb-based materials, which may be related to structural parameter variations as reported previously.[49,50] Under other stimuli such as low-

temperature or with extra pressure, PL may be able to be observed. The PL spectrum for (ETU)SnI_4 is presented in Fig. 4b and has a significantly emission peak at 620 nm under excitation at 532 nm with a wide full width at half maximum (FWHM) of 74 nm, as well as an Stokes shift of 88 nm. This PL band is closely overlapped with the absorption profile and appears to be due to band edge recombination process, in which the photogenerated free excitons (FE) relax back to the valence band. The PL emission energy is generally consistent with the previously reported band edge emission of many 2D tin-iodine perovskites.[28] It is intriguing that (ETU)SnI_4 is the only compound here found to have PL at room temperature, and also the only compound that is composed of ETU with metal iodide with just one composition (Ge and Pb each have two). This may be due to that the dynamics of the organic cations suppress radiative recombination processes in the Ge- and Pb-based phases, whereas the Sn analogue has higher rigidity to maintain the FE emission.

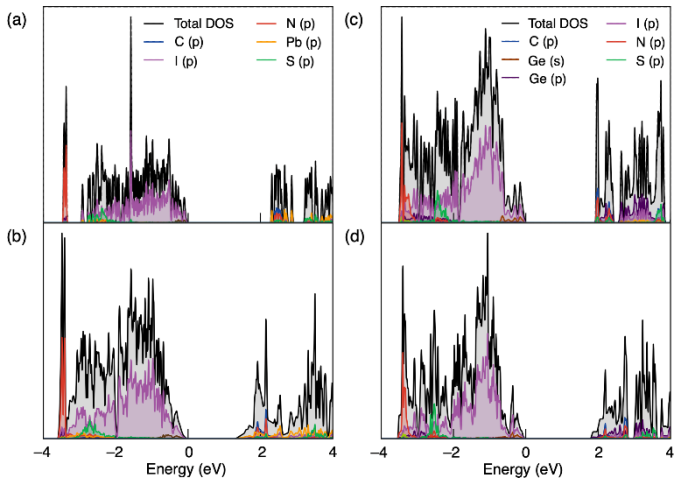

Fig.5 DFT-calculated DOS for (a) (ETU)$_3Pb_2I_{10}$, (b) (ETU)PbI_4, (c) (ETU)$_4Ge_5I_{18}$, and (d) (ETU)GeI_4.

Density functional theory (DFT) calculations were performed in order to gain a better understanding of how the various structure-types presented here affect the electronic structures of these compounds. Fig 5 displays the calculated density of states (DOS) for (ETU)$_3Pb_2I_{10}$, (ETU)PbI_4, (ETU)$_4Ge_5I_{18}$, and (ETU)GeI_4, which allow us to estimate the band gaps of these materials and understand the contribution of different orbitals to the valence and conduction bands. First, considering the Pb series of compounds, we find that the trend in the band gaps is qualitatively similar to what was observed experimentally, with (ETU)PbI_4 having a significantly smaller bandgap than (ETU)$_3Pb_2I_{10}$ (1.22 eV versus 2.22 eV, respectively.) Both band gaps are underestimated compared to experiment, which is typical of DFT calculations using the PBE functional. However, the band gap for (ETU)PbI_4 is underestimated by almost 1 eV, compared with approximately 0.5 eV for (ETU)$_3Pb_2I_{10}$. This discrepancy may be due to the fact that (ETU)PbI_4 is inherently unstable, and the crystal structure used for the calculations needed to be collected at 100 K, versus 298 K for the (ETU)$_3Pb_2I_{10}$ structure. Examining the orbital contributions to the DOS, the valence band edges for both compounds are dominated by the I 5p orbitals with a small contribution from the Pb 6s orbitals. In the case of the conduction band, both compounds show a contribution from the Pb 6p states at the band edges, with a contribution from the ETU orbitals (N 2p, C 2p, and S 3p) slightly higher in energy. The dimensionality of these two compounds manifests itself very clearly in the DOS, where the 0D (ETU)$_3Pb_2I_{10}$ shows a very "spiky" DOS due to the molecular-like nature of its structure, while the 2D (ETU)PbI_4 shows a more continuous curve. In the Ge-based compounds, the band gap trends are again reproduced, where (ETU)$_4Ge_5I_{18}$ has a calculated gap of 1.94 eV and (ETU)GeI_4 has a gap of 1.71 eV. In this case, both band gaps are underestimated by approximately 0.4 eV. The orbital-projected DOS for these compounds shows that, similarly to the lead compounds, the valence band edge is predominately made up of the I 5p orbitals with a small contribution from the Ge 4s orbitals. Interestingly, for (ETU)$_4Ge_5I_{18}$, the edge of the conduction band is dominated by states originating from the ETU cation. These states may be lower in energy compared to those in the other compounds due to the lower C-S-C angle in the ETU cation, which, as previously noted, appears to enhance stability. The DOS for (ETU)GeI_4 shows similar features, but the conduction band edge appears to be primarily comprised of the Ge 4p states and the contributions from the ETU cation are shifted to slightly higher energies. In summary, the DOS for both (ETU)PbI_4 and (ETU)GeI_4 is similar to that of other 2D halide perovskite materials. Additionally, the DOS for (ETU)$_4Ge_5I_{18}$ illustrates how conformational changes in the organic cation can potentially influence the makeup of the band edges in these materials.

Conclusions

In summary, we have synthesized and characterized the structure, optical and electronic properties of five new hybrid iodides by selecting flexible organic species as the stabilizing cations. Among them, two intriguing new "3 × 3" corrugated (110)-oriented type 2D perovskites (ETU)GeI_4 and (ETU)SnI_4 are reported, where (ETU)GeI_4 is the first Ge-based example of the "3×3" type 2D structure. Due to the flexibility of the bond angle of the organic cation, (ETU)PbI_4, featuring conventional (100)-oriented type 2D structure, can be readily transformed into a new yellow-phase 0D structure (ETU)$_3Pb_2I_{10}$. The materials with larger band gaps and lower dimensionality show smaller torsion angles of the organic cations, hinting the movement of the cations are stabilized. Our work highlights the importance of properly manipulate the interactions between the organic and inorganic counterparts, suggesting new design principles for inorganic-organic hybrid halides.

Conflicts of interest

There are no conflicts to declare.

Acknowledgements

This work was supported by the Department of Energy, Office of Science, Basic Energy Sciences, under Grant SC0012541. The work at SUSTech was supported by SUSTech startup grant (Y01216150). The authors are grateful to the assistance of SUSTech Core Research Facilities.

Notes and references

1. A. Kojima, K. Teshima, Y. Shirai and T. Miyasaka, Organometal Halide Perovskites as Visible-Light Sensitizers for Photovoltaic Cells, *J. Am. Chem. Soc.*, 2009, **131**, 6050-6051.
2. N.-G. Park, M. Grätzel, T. Miyasaka, K. Zhu and K. Emery, Towards stable and commercially available perovskite solar cells, *Nat. Energy*, 2016, **1**, 16152.
3. H. J. Snaith, Present status and future prospects of perovskite photovoltaics, *Nat. Mater.*, 2018, **17**, 372-376.
4. C. C. Stoumpos and M. G. Kanatzidis, Halide Perovskites: Poor Man's High-Performance Semiconductors, *Adv. Mater.*, 2016, **28**, 5778-5793.
5. A. Bhui, T. Ghosh, K. Pal, K. Singh Rana, K. Kundu, A. Soni and K. Biswas, Intrinsically Low Thermal Conductivity in the n-Type Vacancy-Ordered Double Perovskite Cs_2SnI_6: Octahedral Rotation and Anharmonic Rattling, *Chem. Mater.*, 2022, **34**, 3301-3310.
6. K. Kundu, P. Dutta, P. Acharyya and K. Biswas, Pb-free layered all-inorganic metal halides $RbSn_2Br_5$: Mechanochemical synthesis, band gap tuning, optical and dielectric properties, *Mater. Res. Bull.,* 2021, **140**, 111339.
7. C. C. Stoumpos and M. G. Kanatzidis, The Renaissance of Halide Perovskites and Their Evolution as Emerging Semiconductors, *Acc. Chem. Res.*, 2015, **48**, 2791-2802.
8. K.-L. Wang, Y.-G. Yang, Y.-H. Lou, M. Li, F. Igbari, J.-J. Cao, J. Chen, W.-F. Yang, C. Dong, L. Li, R.-Z. Tai and Z.-K. Wang, Smelting recrystallization of $CsPbBrI_2$ perovskites for indoor and outdoor photovoltaics, *eScience*, 2021, **1**, 53-59.
9. B. Saparov and D. B. Mitzi, Organic–Inorganic Perovskites: Structural Versatility for Functional Materials Design, *Chem. Rev.*, 2016, **116**, 4558-4596.
10. I. C. Smith, E. T. Hoke, D. Solis-Ibarra, M. D. McGehee and H. I. Karunadasa, A Layered Hybrid Perovskite Solar-Cell Absorber with Enhanced Moisture Stability, *Angew. Chem. Int. Ed.*, 2014, **53**, 11232-11235.
11. C. C. Stoumpos, D. H. Cao, D. J. Clark, J. Young, J. M. Rondinelli, J. I. Jang, J. T. Hupp and M. G. Kanatzidis, Ruddlesden–Popper Hybrid Lead Iodide Perovskite 2D Homologous Semiconductors, *Chem. Mater.*, 2016, **28**, 2852-2867.
12. L. Mao, W. Ke, L. Pedesseau, Y. Wu, C. Katan, J. Even, M. R. Wasielewski, C. C. Stoumpos and M. G. Kanatzidis, Hybrid Dion–Jacobson 2D Lead Iodide Perovskites, *J. Am. Chem. Soc.*, 2018, **140**, 3775-3783.
13. L. Mao, C. C. Stoumpos and M. G. Kanatzidis, Two-Dimensional Hybrid Halide Perovskites: Principles and Promises, *J. Am. Chem. Soc.*, 2019, **141**, 1171-1190.
14. P. Acharyya, K. Kundu and K. Biswas, 2D layered all-inorganic halide perovskites: recent trends in their structure, synthesis and properties, *Nanoscale*, 2020, **12**, 21094-21117.
15. C. C. Stoumpos, L. Mao, C. D. Malliakas and M. G. Kanatzidis, Structure–Band Gap Relationships in Hexagonal Polytypes and Low-Dimensional Structures of Hybrid Tin Iodide Perovskites, *Inorg. Chem.*, 2017, **56**, 56-73.
16. L. Mao, P. Guo, M. Kepenekian, I. Hadar, C. Katan, J. Even, R. D. Schaller, C. C. Stoumpos and M. G. Kanatzidis, Structural Diversity in White-Light-Emitting Hybrid Lead Bromide Perovskites, *J. Am. Chem. Soc.*, 2018, **140**, 13078-13088.
17. H. Lin, C. Zhou, Y. Tian, T. Siegrist and B. Ma, Low-Dimensional Organometal Halide Perovskites, *ACS Energy Lett.*, 2018, **3**, 54-62.
18. M. I. Saidaminov, O. F. Mohammed and O. M. Bakr, Low-Dimensional-Networked Metal Halide Perovskites: The Next Big Thing, *ACS Energy Lett.*, 2017, **2**, 889-896.
19. L. Mao, Y. Wu, C. C. Stoumpos, M. R. Wasielewski and M. G. Kanatzidis, White-Light Emission and Structural Distortion in New Corrugated Two-Dimensional Lead Bromide Perovskites, *J. Am. Chem. Soc.*, 2017, **139**, 5210-5215.
20. E. R. Dohner, E. T. Hoke and H. I. Karunadasa, Self-Assembly of Broadband White-Light Emitters, *J. Am. Chem. Soc.*, 2014, **136**, 1718-1721.
21. E. R. Dohner, A. Jaffe, L. R. Bradshaw and H. I. Karunadasa, Intrinsic White-Light Emission from Layered Hybrid Perovskites, *J. Am. Chem. Soc.*, 2014, **136**, 13154-13157.
22. Y. Y. Li, C. K. Lin, G. L. Zheng, Z. Y. Cheng, H. You, W. D. Wang and J. Lin, Novel <110>-Oriented Organic−Inorganic Perovskite Compound Stabilized by N-(3-Aminopropyl)imidazole with Improved Optical Properties, *Chem. Mater.*, 2006, **18**, 3463-3469.
23. M.-H. Tremblay, F. Thouin, J. Leisen, J. Bacsa, A. R. Srimath Kandada, J. M. Hoffman, M. G. Kanatzidis, A. D. Mohite, C. Silva, S. Barlow and S. R. Marder, $(4NPEA)_2PbI_4$ (4NPEA = 4-Nitrophenylethylammonium): Structural, NMR, and Optical Properties of a 3 × 3 Corrugated 2D Hybrid Perovskite, *J. Am. Chem. Soc.*, 2019, **141**, 4521-4525.
24. Y.-Y. Guo, L.-J. Yang, S. Biberger, J. A. McNulty, T. Li, K. Schötz, F. Panzer and P. Lightfoot, Structural Diversity in Layered Hybrid Perovskites, A_2PbBr_4 or $AA'PbBr_4$, Templated by Small Disc-Shaped Amines, *Inorg. Chem.*, 2020, **59**, 12858-12866.
25. B. Febriansyah, T. M. Koh, Y. Lekina, N. F. Jamaludin, A. Bruno, R. Ganguly, Z. X. Shen, S. G. Mhaisalkar and J. England, Improved Photovoltaic Efficiency and Amplified Photocurrent Generation in Mesoporous n = 1 Two-Dimensional Lead–Iodide Perovskite Solar Cells, *Chem. Mater.*, 2019, **31**, 890-898.
26. B. Febriansyah, Y. Lekina, J. Kaur, T. J. N. Hooper, P. C. Harikesh, T. Salim, M. H. Lim, T. M. Koh, S. Chakraborty, Z. X. Shen, N. Mathews and J. England, Formation of Corrugated n = 1 2D Tin Iodide Perovskites and Their Use as Lead-Free Solar Absorbers, *ACS Nano*, 2021, **15**, 6395-6409.
27. J. Guan, Z. Tang and A. M. Guloy, α-$[NH_3(CH_2)_5NH_3]SnI_4$: a new layered perovskite structure, *Chem. Commun.*, 1999, 1833-1834.

28. L. Mao, H. Tsai, W. Nie, L. Ma, J. Im, C. C. Stoumpos, C. D. Malliakas, F. Hao, M. R. Wasielewski, A. D. Mohite and M. G. Kanatzidis, Role of Organic Counterion in Lead- and Tin-Based Two-Dimensional Semiconducting Iodide Perovskites and Application in Planar Solar Cells, *Chem. Mater.*, 2016, **28**, 7781-7792.
29. C. C. Stoumpos, L. Frazer, D. J. Clark, Y. S. Kim, S. H. Rhim, A. J. Freeman, J. B. Ketterson, J. I. Jang and M. G. Kanatzidis, Hybrid Germanium Iodide Perovskite Semiconductors: Active Lone Pairs, Structural Distortions, Direct and Indirect Energy Gaps, and Strong Nonlinear Optical Properties, *J. Am. Chem. Soc.*, 2015, **137**, 6804-6819.
30. D. B. Mitzi, Synthesis, Crystal Structure, and Optical and Thermal Properties of $(C_4H_9NH_3)_2MI_4$ (M = Ge, Sn, Pb), *Chem. Mater.*, 1996, **8**, 791-800.
31. R. Chiara, M. Morana, M. Boiocchi, M. Coduri, M. Striccoli, F. Fracassi, A. Listorti, A. Mahata, P. Quadrelli, M. Gaboardi, C. Milanese, L. Bindi, F. De Angelis and L. Malavasi, Role of spacer cations and structural distortion in two-dimensional germanium halide perovskites, *J. Mater. Chem. C*, 2021, **9**, 9899-9906.
32. G. Sheldrick, Crystal structure refinement with SHELXL, *Acta Crystallogr., Sect. C: Struct. Chem.*, 2015, **71**, 3-8.
33. G. Sheldrick, SHELXT - Integrated space-group and crystal-structure determination, *Acta Crystallogr., Sect. A: Found. Adv.*, 2015, **71**, 3-8.
34. O. V. Dolomanov, L. J. Bourhis, R. J. Gildea, J. A. K. Howard and H. Puschmann, OLEX2: a complete structure solution, refinement and analysis program, *J. Appl. Crystallogr.*, 2009, **42**, 339-341.
35. G. Kortüm, W. Braun and G. Herzog, Principles and Techniques of Diffuse-Reflectance Spectroscopy, *Angew. Chem. Int. Ed. Engl.*, 1963, **2**, 333-341.
36. G. Kresse and J. Hafner, Ab initio molecular-dynamics simulation of the liquid-metal--amorphous-semiconductor transition in germanium, *Phys. Rev. B*, 1994, **49**, 14251-14269.
37. G. Kresse and J. Furthmüller, Efficiency of ab-initio total energy calculations for metals and semiconductors using a plane-wave basis set, *Comput. Mater. Sci.*, 1996, **6**, 15-50.
38. G. Kresse and J. Furthmüller, Efficient iterative schemes for ab initio total-energy calculations using a plane-wave basis set, *Phys. Rev. B*, 1996, **54**, 11169-11186.
39. J. P. Perdew, K. Burke and M. Ernzerhof, Generalized Gradient Approximation Made Simple, *Phys. Rev. Lett.*, 1996, **77**, 3865-3868.
40. P. E. Blöchl, Projector augmented-wave method, *Phys. Rev. B*, 1994, **50**, 17953-17979.
41. G. Kresse and D. Joubert, From ultrasoft pseudopotentials to the projector augmented-wave method, *Phys. Rev. B*, 1999, **59**, 1758-1775.
42. H. J. Monkhorst and J. D. Pack, Special points for Brillouin-zone integrations, *Phys. Rev. B*, 1976, **13**, 5188-5192.
43. Y. Hinuma, G. Pizzi, Y. Kumagai, F. Oba and I. Tanaka, Band structure diagram paths based on crystallography, *Comput. Mater. Sci.*, 2017, **128**, 140-184.
44. A. Togo and I. Tanaka, *Spglib : a software library for crystal symmetry search*, 2018.
45. S. P. Ong, W. D. Richards, A. Jain, G. Hautier, M. Kocher, S. Cholia, D. Gunter, V. L. Chevrier, K. A. Persson and G. Ceder, Python Materials Genomics (pymatgen): A robust, open-source python library for materials analysis, *Comput. Mater. Sci.*, 2013, **68**, 314-319.
46. S. Grimme, Semiempirical GGA-type density functional constructed with a long-range dispersion correction, *J. Comput. Chem.*, 2006, **27**, 1787-1799.
47. R. Bakthavatsalam, M. P. U. Haris, S. R. Shaikh, A. Lohar, A. Mohanty, D. Moghe, S. Sharma, C. Biswas, S. S. K. Raavi, R. G. Gonnade and J. Kundu, Ligand Structure Directed Dimensionality Reduction (2D→1D) in Lead Bromide Perovskite, *J. Phys. Chem. C*, 2020, **124**, 1888-1897.
48. P.-P. Sun, D. R. Kripalani, M. Hao, W. Chi, W. Li and K. Zhou, Emissive Nature and Molecular Behavior of Zero-Dimensional Organic–Inorganic Metal Halides $Bmpip_2MX_4$, *J. Phys. Chem. Lett.* 2020, **11**, 5234-5240.
49. X. Lü, C. Stoumpos, Q. Hu, X. Ma, D. Zhang, S. Guo, J. Hoffman, K. Bu, X. Guo, Y. Wang, C. Ji, H. Chen, H. Xu, Q. Jia, W. Yang, M. G. Kanatzidis and H.-K. Mao, Regulating off-centering distortion maximizes photoluminescence in halide perovskites, *Natl Sci Rev,* 2020, **8**, nwaa288.
50. M. Morana, R. Chiara, B. Joseph, T. B. Shiell, T. A. Strobel, M. Coduri, G. Accorsi, A. Tuissi, A. Simbula, F. Pitzalis, A. Mura, G. Bongiovanni and L. Malavasi, Pressure response of decylammonium-containing 2D iodide perovskites, *iScience*, 2022, **25**, 104057.

ARTICLE

TOC

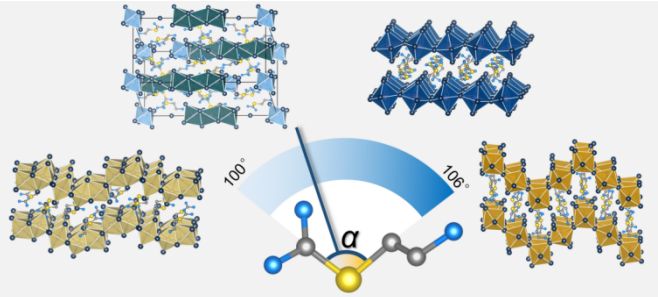

By using S-(2-aminoethyl)isothiouronium (ETU) as the templating cation, five new metal iodide hybrids are reported. (ETU)GeI_4, (ETU)$_4Ge_5I_{18}$, (ETU)PbI_4 and (ETU)$_3Pb_2I_{10}$ are synthesized with different stoichiometrics and exhibiting different C-S-C angles in the organic cation.

Supporting Information (SI):

“Breathing” organic cation to stabilize multiple structures in low-dimensional Ge-, Sn-, and Pb-based hybrid iodide perovskites

Congcong Chen,[a] Emily E. Morgan,[b] Yang Liu,[a] Jian Chen,[a] Ram Seshadri[b] and Lingling Mao*[a]

a Department of Chemistry, Southern University of Science and Technology, Shenzhen, 518055, P. R. China

b Materials Research Laboratory and Materials Department, University of California, Santa Barbara, California 93106, United States

Section I. Crystallographic tables

Table S1. Crystal data and structure refinement for $(ETU)_4Ge_5I_{18}$, $(ETU)GeI_4$ and $(ETU)SnI_4$ at 298 K.

Compound	$(ETU)_4Ge_5I_{18}$	$(ETU)GeI_4$	$(ETU)SnI_4$
Formula	$C_{12}H_{44}Ge_5I_{18}N_{12}S_4$	$C_3H_{11}GeI_4N_3S$	$C_3H_{11}I_4N_3SSn$
M_r / g·mol^{-1}	3131.98	701.40	747.50
T (K)	298	298	298
Crystal System	Triclinic	Orthorhombic	Orthorhombic
Space Group	*P*-1	*Pbca*	*Pbca*
a / Å	8.6160(5)	19.178(3)	19.472(4)
b / Å	10.9195(6)	12.2635(17)	12.509(2)
c / Å	18.0200(11)	25.280(4)	25.392(4)
α / °	81.199(2)	90	90
β / °	87.561(2)	90	90
γ / °	70.561(2)	90	90
V / Å^3	1579.84(16)	5945.7(15)	6185.2(19)
Z	1	16	16
ρ_{calcd} (g·cm^{-3})	3.292	3.134	3.211
μ (mm^{-1})	11.303	10.477	9.742
F (000)	1378	4960	5248
Reflections collected	19386	41787	6325
Independent reflections	5808	5466	220
GOF on F^2	1.232	1.204	1.031
R_1, wR_2 [$I \geq 2\sigma(I)$][a]	0.0466/0.1144	0.0366, 0.0869	0.0569, 0.1046
R_1, wR_2 (all data)[b]	0.0528/0.1190	0.0528, 0.0999	0.1537, 0.1392
Largest diff. peak/hole (e Å^{-3})	1.32/-4.85	2.09/-3.61	1.27/-1.65

[a] $R_1 = \Sigma||F_o| - |F_c||/\Sigma|F_o|$. [b] $wR_2 = [\Sigma w(F_o^2 - F_c^2)^2/\Sigma w(F_o^2)^2]^{1/2}$

Table S2. Crystal data and structure refinement for (ETU)PbI_4 at 100 K and $(ETU)_3Pb_2I_{10}$ at 298 K.

Compound	(ETU)PbI_4	$(ETU)_3Pb_2I_{10}$
Formula	$C_3H_{11}I_4N_3PbS$	$C_9H_{33}I_{10}N_9Pb_2S_3$
M_r / g·mol^{-1}	836.00	2047.02
T (K)	100	298
Crystal System	Monoclinic	Trigonal
Space Group	$P2_1/c$	R-3
a / Å	12.2987(6)	15.0135(19)
b / Å	12.5368(6)	15.0135(19)
c / Å	19.8230(10)	31.781(4)
α / °	90	90
β / °	92.204(2)	90
γ / °	90	120
V / Å^3	3054.2(3)	6203.8(18)
Z	8	6
ρ_{calcd} (g·cm^{-3})	3.636	3.287
μ (mm^{-1})	19.240	15.764
F (000)	2880	5352
Reflections collected	43292	5926
Independent reflections	5607	4081
GOF on F^2	1.024	0.985
R_1, wR_2 [$I \geq 2\sigma(I)$][a]	0.0713, 0.1898	0.0398, 0.0920
R_1, wR_2 (all data)[b]	0.0779, 0.1962	0.0581, 0.0997
Largest diff. peak/hole (e Å^{-3})	6.99/-10.76	1.84/-3.75

[a] $R_1 = \Sigma||F_o| - |F_c||/\Sigma|F_o|$. [b] $wR_2 = [\Sigma w(F_o^2 - F_c^2)^2/\Sigma w(F_o^2)^2]^{1/2}$

Table S3. Structural parameters for the low dimensional perovskites in this work.

Compounds	Space group	Metals	Δd (bond length distortion index)	σ^2 (bond angle variance)
$(ETU)_4Ge_5I_{18}$	*P*-1	Ge1	0.00522	6.3326
		Ge2	0.05874	11.3104
		Ge3	0.06004	18.8684
$(ETU)GeI_4$	*Pbca*	Ge1	0.08157	27.3030
		Ge2	0.08235	23.7656
$(ETU)SnI_4$	*Pbca*	Sn1	0.02521	6.4817
		Sn2	0.03848	19.0447
$(ETU)PbI_4$	$P2_1/c$	Pb1	0.01091	3.0167
		Pb2	0.01460	7.6529
$(ETU)_3Pb_2I_{10}$	*R*-3	Pb1	0.00850	16.2803
		Pb2	0.00000	95.8555
		Pb3	0.00000	0.7449

Table S4. M-I-M angles in $(ETU)_4Ge_5I_{18}$, $(ETU)GeI_4$, $(ETU)SnI_4$, $(ETU)PbI_4$ and $(ETU)_3Pb_2I_{10}$.

Compound	Labels	Angles (°)
$(ETU)_4Ge_5I_{18}$	Ge(1)-I(2)-Ge(2)	161.88(3)
	Ge(2)-I(7)-Ge(3)	68.49(3)
	Ge(2)-I(6)-Ge(3)	75.96(3)
	Ge(2)-I(1)-Ge(1)	171.39(3)
	Ge(2)-I(5)-Ge(3)	78.04(3)
$(ETU)GeI_4$	Ge(1)-I(7)-Ge(2)	162.14(3)
	Ge(2)-I(5)-Ge(1)	162.06(3)
	Ge(2)-I(6)-Ge(2)	157.40(3)
	Ge(1)-I(3)-Ge(1)	167.58(4)
$(ETU)SnI_4$	Sn(2)-I(3)-Sn(1)	167.06(5)
	Sn(2)-I(7)-Sn(2)	168.39(6)
	Sn(1)-I(1)-Sn(2)	159.25(5)
	Sn(1)-I(2)-Sn(1)	155.42(5)
$(ETU)PbI_4$	Pb(2)-I(2)-Pb(1)	146.06(5)
	Pb(1)-I(3)-Pb(1)	154.50(5)

Section II. Simulated and experimental powder X-ray diffraction (PXRD) patterns

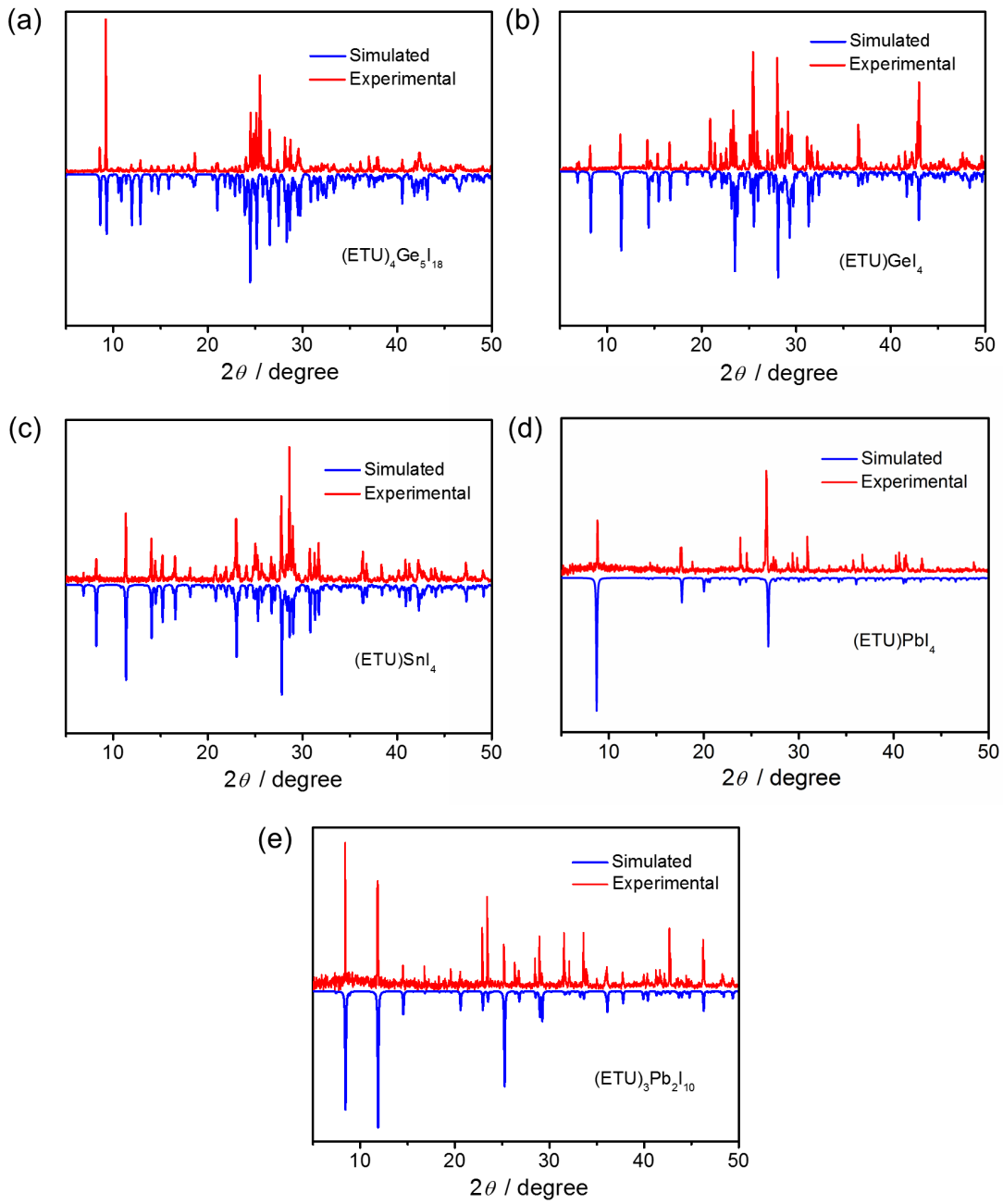

Fig. S1 Comparison of the experimental and simulated PXRD patterns for $(ETU)_4Ge_5I_{18}$ (a), $(ETU)GeI_4$ (b), $(ETU)SnI_4$ (c), $(ETU)PbI_4$ (d) and $(ETU)_3Pb_2I_{10}$ (e). Due to the large size of the crystal in test for $(ETU)PbI_4$, the crystal anisotropy along the (110) crystal face is more prominent.

Section III. Extra structural illustrations

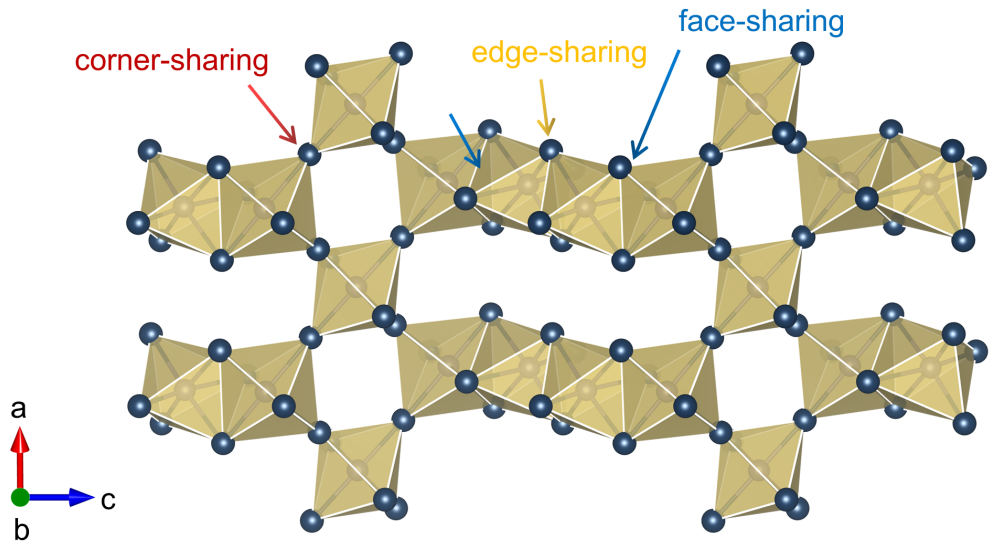

Fig. S2 Inorganic layer configuration of $(ETU)_4Ge_5I_{18}$ along the b axis. Arrow symbol: blue (face-sharing), yellow (edge-sharing), red (corner-sharing).

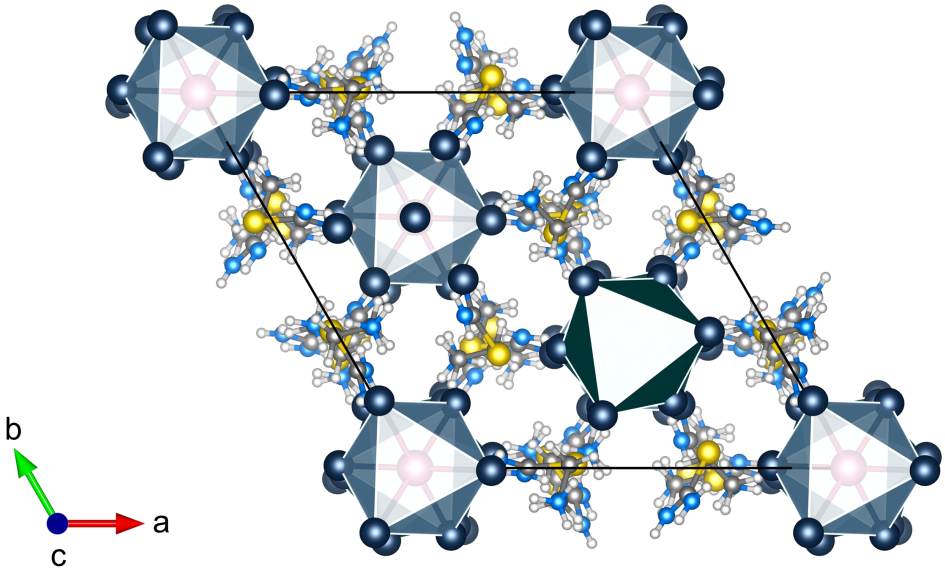

Fig. S3 Crystal structures of $(ETU)_3Pb_2I_{10}$ along the c axis.